Polymer Chemistry

Accepted Manuscript

ROYAL SOCIETY OF CHEMISTRY

www.rsc.org/polymers

Solution-Processed Small Molecules Based on Benzodithiophene and Difluorobenzothiadiazole for Inverted Organic Solar Cells

Xunfan Liao[a], Feiyan Wu[a], Lie Chen*[a,b] and Yiwang Chen[a,b]

[a]College of Chemistry/Institute of Polymers, Nanchang University, 999 Xuefu Avenue, Nanchang 330031, China

[b]Jiangxi Provincial Key Laboratory of New Energy Chemistry, Nanchang University, 999 Xuefu Avenue, Nanchang 330031, China

*Corresponding author. Tel.: +86 791 83968703; fax: +86 791 83968830. E-mail: chenlie@ncu.edu.cn (L. Chen).

Xunfan Liao and Feiyan Wu contributed equally to this work.

Abstract

The monofluorinated small molecule has been proved to be a promising donor for high performance small molecular solar cells (SMSCs). Herein, two solution-processable acceptor-donor-acceptor (A-D-A) type small molecules (SMs) with 4,8-bis(5-hexylthiophen-2-yl)benzo[1,2-b:4,5-b']dithiophene (BDTT) as donor core and benzothiadiazole (BT) or difluoro-2,1,3-benzothiadiazole (DFBT) as acceptor unit, namely BDT(TBTTT6)$_2$ and BDT(TffBTTT6)$_2$ respectively, are designed and synthesized to extensively investigate the effect of fluorination on the optoelectronic properties, molecular organization, and photovolatic performance in SMSCs. The fluorinated BDT(TffBTTT6)$_2$ shows the relatively broader and stronger absorbance, more favorable molecular packing and deeper highest occupied molecular orbital (HOMO) energy level than nonfluorinated BDT(TBTTT6)$_2$, leading to a higher open-circuit voltage (V_{oc}), circuit current (J_{sc}), fill factor (FF), and hole mobility in SMSCs. Additionally, the power conversion efficiency (PCE) are significantly improved from 1.76% to 4.17% for BDT(TffBTTT6)$_2$ and from 1.3% to 3.17% for BDT(TBTTT6)$_2$ based inverted devices after optimizing by 1,8-diiodooctane (DIO) and thermal annealing (TA). It should be noted that the PCE of 4.17% is the highest reported value for the solution-processed inverted SMSCs based on BDT and BT unit. Grazing incident X-ray diffraction (GIXRD), transmission electron microscopy (TEM) and atomic force microscopy (AFM) demonstrate that the fluorinated small molecule optimization by DIO and thermal annealing promote a more well-intermixed microphase morphology as well as better donor/acceptor interpenetrating network in active film for more efficient charge transfer and transportation than nonfluorinated one, leading to the dramatically improvement in device performance. These results unambiguously demonstrate that the introduction of F atoms into molecular backbone as well as optimizing by solvent additive process can be an effective strategy for the development of electron-donating materials for stabilized inverted-based SMSCs.

1. Introduction

Solution-processed bulk-heterojunction (BHJ) organic solar cells (OSCs) have attracted great attention recently for their promising applications as a competitive technology of environment friendly renewable energy and for its advantages of low cost, lightweight, and flexibility.[1-5] Currently, the electron donor materials in active layer for OSCs have been divided into two types, polymer donor and small molecule donor. In the past decades, though the power conversion efficiencies (PCEs) of the polymer-based solar cells (PSCs) have been achieved over 10%,[6-9] solution-processed small molecular solar cells (SMSCs) still drawn more and more attention in recent years due to its promising advantages of easily structure design, well-defined structure thus less batch-to-batch variation and easily refine, and their PCEs almost reached an equal value to the PSCs.[10-12]

Recently, the planar linear A-D-A structured small molecules based on thiophene,[13,14] benzo[1,2-b:4,5-b']dithiophene (BDT),[15-19] or dithieno[3,2-b:2',3'-d]silole (DTS)[20,21] as donor cores, benzo[c][1,2,5]thiadiazole (BT),[22] diketopyrrolopyrrole (DPP),[23] thienopyrroledione (TPD),[24] or dye building blocks[13-18] as acceptor units have been intensively researched. Among these donor cores, benzo-[1,2-b:4,5-b']dithiophene (BDT) has been successfully developed as an electron-donating unit for its large planar structure, low deeper highest occupied molecular orbital (HOMO) energy level, high hole mobility, and good photovoltaic performance both in SMSCs and PSCs.[25-27] For the acceptor units, BT has been very popular in constructing low-band-gap conjugated polymers owing to its strong electron accepting ability and commercial availability.[28,29] Otherwise, these two N atoms in the thiadiazole ring could possibly form hydrogen bonding with adjacent units leading to a more planar backbone. Many polymers with a BT acceptor unit have shown low band gaps and good photovoltaic properties.[25,26]

Usually, to obtain better performance, the small molecules (SMs) donors' structure need to be optimized. The strategies used for the design of high performance conjugated polymers could also be applied to the molecular design of SMs. The method of introduction of fluorine (F) atoms onto conjugated polymer backbone has been proven to be an effective way to improve the performance of BHJ solar cells.[30-38] Owing to the electron-withdrawing character of F atom, conjugated polymers with F atoms usually exhibit lower HOMO energy levels, thus lead to increased open circuit voltage (V_{oc}) of the corresponding device.[32] Moreover, fluorination can increase other photovoltaic properties, such as the short circuit current (J_{sc}), fill factor (FF),[35] and hole mobility.[39] Thereby, it is reported that the monofluorinated small molecule has also been proved to be a promising donor for high performance small SMSCs,[21] but the effect of fluorination on the optoelectronic properties, molecular organization, and photovolatic performance of small molecular device has not been investigated extensively.

In addition, the device structure is another vital factor to achieve better performance of SMSCs. A conventional BHJ PSCs and SMSCs with an active layer sandwiched by a low work-function aluminum cathode and a hole-conducting poly(3,4-ethylenedioxylenethiophene):poly(styrenesulfonic acid) (PEDOT:PSS) layer on top of an indium tin oxide (ITO) substrate is the most widely used and researched device configuration. Compared to conventional device, inverted solar cell architectures are becoming increasingly attractive by allowing more air stable, higher work function metal electrodes (e.g., Ag) to be used, resulting in a longer-lived device. However, the present small molecular donor materials were rarely applied for SMSCs with an inverted device. So it is necessary to design and synthesize new small molecules for high performance inverted SMSCs.

Inspired by the advantages of fluorinated molecules and inverted device structure, in this work, we design and synthesize fluorinated acceptor-donor-acceptor (A-D-A) type small molecules BDT(TffBTTT6)$_2$ based on 4,8-bis(5-hexylthiophen-2-yl)benzo[1,2-b:4,5-b']dithiophene (BDTT) donor core and difluoro-2,1,3-benzothiadiazole (DFBT) acceptor unit for inverted SMSCs (**Scheme 1**). And the nonfluorinated analogues BDT(TBTTT6)$_2$ is also prepared for comparison. Hexylbithiophene end-capping unit is incorporated to fine control the optical and electronic properties of the two molecules.[40] The effect of fluorination on the properties of SMs and their corresponding device performance have been systematically investigated. As expected, both of SMs exhibit broad absorption in the visible region and high thermal stability. Fluorinated BDT(TffBTTT6)$_2$ shows better performance than nonfluorinated BDT(TBTTT6)$_2$, resulting from the broader absorbance, higher hole mobility, and deeper HOMO energy level. However, when blended with the acceptor [6,6]-phenyl-C_{61}-butyric acid methyl ester ($PC_{61}BM$) or [6,6]-phenyl-C_{71}-butyric acid methyl ester ($PC_{71}BM$), SMSCs only deliver very low PCE, due to the poor morphology of blend film in BHJ solar cells. After treated with1,8-diiodooctane (DIO) additive and annealed at 70 °C, the PCEs are significantly improved from 1.76% to 4.17% for BDT(TffBTTT6)$_2$/$PC_{61}BM$ and from 1.3% to 3.17% for BDT(TBTTT6)$_2$/$PC_{71}BM$ based SMSCs. It should be looked out that the PCE of 4.17% is the highest reported value for the solution-processed inverted SMSCs based

on BDT and BT unit. Grazing incident X-ray diffraction (GIXRD), transmission electron microscopy (TEM) and atomic force microscopy (AFM) demonstrate that for BDT(TffBTTT6)$_2$ and BDT(TBTTT6)$_2$, optimization by DIO and thermal annealing promote favorable morphology evolution of active layer, especially for the fluorinated BDT(TffBTTT6)$_2$, contribution to the dramatically improvement of device performance.

2. Result and Discussion

2.1. Synthesis. The synthetic route of two small molecules, BDT(TffBTTT6)$_2$ and BDT(TBTTT6)$_2$ are presented in **Scheme 1**, and the detailed synthesis of the molecules are provided in experimental section. 2-Hexyl-5-(tributylstannyl)thiophene (compound **1**) prepared according to the reported literature[41] was reacted with 4,7-bis(5-bromothiophene-2-yl)-5,6-difluorobenzo[c][1,2,5]thiadiazole (compound **2**) and 4,7-bis(2-bromo-5-thien)-2,1,3-benzothiadiazole (compound **3**) to afford compound **4** and compound **5**, respectively. Through the Still cross-coupling reaction, the fluorinated BDT(TffBTTT6)$_2$ and non-fluorinated BDT(TBTTT6)$_2$ were obtained by compound **4** and compound **5** reacting with 2,6-bis(trimethyltin)-4,8-bis(5-(2-ethylhexy)thiophen-2-yl)benzo[1,2-b:4,5-b']dithiophene (compound **6**), respectively. The final products are soluble in common organic solvents, such as chloroform, tetrahydrofuran, chlorobenzene and 1,2-dichlorobenzene. The structures of the compounds have been fully confirmed by structural analysis, as shown in **Figure S1-6** (Supporting Information).

2.2. Thermal Properties. The thermal stability of the small molecules was investigated by thermogravimetric analysis (TGA) under nitrogen atmosphere at a heating rate of 10 °C min^{-1}, as shown in **Figure S7**. Two small molecules exhibit excellent thermal stability for long-term photovoltaic application with 5% weight loss temperature (T_d) over 400 °C. In addition, the similar T_d of two small molecules indicates that the introduction of two fluorine atoms in the 5,6-positions of BT does not affect the thermal stability. Thermal behavior of the two small molecules has been further studied by differential scanning calorimetry (DSC). As shown in **Figure S8** in the Supporting Information, BDT(TffBTTT6)$_2$ and BDT(TBTTT6)$_2$ exhibit endothermic peaks at 225.3 °C, 205 °C upon heating, respectively, corresponding to melting temperature (T_m) caused by the melting of the compounds backbone. The crystallization peaks at 155.1 °C for BDT(TffBTTT6)$_2$ and 164.3 °C for BDT(TBTTT6)$_2$ while cooling from the melting state.

2.3. Absorption Spectra. The absorption spectra of the SMs solution and films are presented in **Figure 1** and the correlated optical parameters are summarized in **Table 1**. Benefited from their appropriate conjugation length (9 conjugated units) and D-A molecular structures with BDT and BT, the absorption spectra of the compounds in chloroform solutions show a broad absorption in the wavelength range from 300 nm to 650 nm (see **Figure 1**). The absorption bands have a high and a low energy bands, which is attributed to localized π-π* transitions and internal charge transfer transitions, respectively. In the solid state, a distinct bathochromic shift by ca. 100 nm for both SMs compared to their absorption in solution. And a new vibronic peak in the low energy transition region emerged, revealing the strong π-π stacking interaction existing in the solid films. Relative to the BDT(TBTTT6)$_2$, the fluorinated BDT(TffBTTT6)$_2$ shows broader absorption band with enhanced intensity, even extending to 800 nm. The enhanced absorption at the visible region results from the improved intra-molecular chain interaction by incorporation of two fluorine (F) atoms onto conjugated SMs backbone, which would increase the short circuit current (J_{sc}) in the devices. As shown in **Table 1**, the optical band gaps (Eg^{opt}) can be calculated to be 1.61 and 1.74 eV from the absorption edges of BDT(TffBTTT6)$_2$ and films BDT(TBTTT6) (ca. 769 and 714 nm), respectively.

2.4. Electrochemical Properties. The highest occupied molecular orbital (HOMO) and lowest unoccupied molecular orbital (LUMO) energy levels of SMs were investigated by Cyclic voltammetry (CV). The CV

measurements were conducted in a 0.1 M Bu_4PF_6/CH_3CN solution. The platinum disc working electrode was coated with the SMs thin film by using chloroform solution. The cyclic voltammograms of the two small molecules films are shown in **Figure 2a**. The onset oxidation potentials (E_{ox}) and onset reduction potentials (E_{red}) are 1.02 V and -0.61 V vs Ag/AgCl for BDT(TffBTTT6)$_2$, and 0.92 V and -0.78 V vs Ag/AgCl for BDT(TBTTT6)$_2$. The HOMO and LUMO energy levels of the SMs films are estimated from the E_{ox} and E_{red} values according to the following equations: HOMO = -e(E_{ox} + 4.4) (eV), and LUMO = -e(E_{red} + 4.4) (eV), where the potential values of E_{ox} and E_{red} are versus Ag/AgCl. Therefore, the HOMO for BDT(TffBTTT6)$_2$ and BDT(TBTTT6)$_2$ are calculated to be -5.42 and -5.32 eV, and the LUMO for BDT(TffBTTT6)$_2$ and BDT(TBTTT6)$_2$ are calculated to be -3.79 and -3.62 eV, respectively (see **Table 1**). The electrochemical band gaps are found to be 1.63 eV for BDT(TffBTTT6)$_2$ and 1.70 eV for BDT(TBTTT6)$_2$, which are well consistent with the values from absorption measurements. From the data we can see that introduction of fluorine atoms can effectively reduce both HOMO and bandgap of BDT(TffBTTT6)$_2$, therefore, an improved V_{oc} in BHJ solar cells can be anticipated. The energy levels of BDT(TffBTTT6)$_2$ and BDT(TBTTT6)$_2$ in BHJ solar cells are illustrated in **Figure 2b**.

2.5. Computational Calculation. In order to deeply understand the minimum-energy conformations and molecular orbital distributions by introduction of F atoms, the structures of the SMs were computed by using density functional theory (DFT) calculation at B3LYP/6-31G level with the Gaussian 09 package. DFT calculations are useful for predicting optimized structures, confirming molecular geometry, verifying complete delocalization across the conjugated backbones, and predicting electronic energy levels.[42] The alkyl groups are replaced by methyl groups for simplicity, but the electronic properties and equilibrium geometries will not be influenced significantly.[43] The energetically stable molecular geometry with the lowest total energy in each single basic unit is shown in **Figure 3a** and **c**. The dihedral angles between dithienylbenzothiadiazole (DTBT) unit and the BDT units in BDT(TBTTT6)$_2$ are calculated to be 7.0° (outward direction) and -6.9° (inward direction), while the dihedral angles between dithienyl-difluorobenzothiadiazole (DT2FBT) unit and the BDT units in BDT(TffBTTT6)$_2$ are 7.4° (outward direction) and -6.8° (inward direction). Thus both of the interfacial angles in BDT(TffBTTT6)$_2$ and BDT(TBTTT6)$_2$ are ~14°, contributing to forming high molecular planarity. The molecular orbital distributions of HOMO and LUMO isosurfaces for each model are shown in **Figure 3b** and **d**. HOMO for both the models are well-delocalized over the whole conjugated backbone, while LUMO are mainly distributed on the electron accepting BT blocks. Moreover, the calculated HOMO and LUMO level of fluorinated-based small molecule BDT(TffBTTT6)$_2$ are lower than those of BDT(TBTTT6)$_2$, which is in agreement with the results of Cyclic voltammetry instrument.

From the DFT calculation, the impact of F atoms on the molecular packing can not be clearly detected. To obtain deeper insight of the molecular stacking of the small molecules films, X-ray diffraction (XRD) analysis of the SMs thin films was thus performed (see **Figure 4**). Both of SMs show one strong diffraction peak at small angle region and one broad diffraction peak at wide angle region. The diffraction peaks of BDT(TffBTTT6)$_2$ and BDT(TBTTT6)$_2$ at small angle region are located at 2θ = 4.68° and 3.96°, corresponding to the d-spacing between the molecular layers of 2.10 and 2.48 nm, respectively. The smaller d-spacing of the fluorinated BDT(TffBTTT6)$_2$ than BDT(TBTTT6)$_2$ is related to the increased inter- or intra-molecular interactions from F-H, F-F interactions.

2.6. Bulk-Heterojunction Solar Cell Performance. To investigate the photovoltaic properties of the SMs, bulk-heterojunction SMSCs were fabricated with the organic molecules as donor (D) and $PC_{61}BM$ or $PC_{71}BM$ as acceptor (A) in the inverted device structure of ITO/ZnO/active layer/MoO_3/Ag. The active layers were spin-coated from their chloroform solutions with the thickness of ~110 nm. The optimized *J-V* curves are shown in **Figure 5** and the corresponding photovoltaic performance is summarized in **Table 2**. We first performed the optimization

of photovoltaic performance of the SMSCs based on BDT(TffBTTT6)$_2$ as donor and $PC_{71}BM$ as acceptor by changing D/A weight ratios from 1:1.5 to 1.5:1. As shown in **Figure S9** and **Table S1**, the device with the D/A weight ratio of 1:0.8 shows the best power conversion efficiency (PCE) of 1.3% with an open circuit voltage (V_{oc}) of 0.73 V, a low short-circuit current density (J_{sc}) of 2.97 mA/cm^2 and a fill factor (FF) of 59.8%. By replacing $PC_{71}BM$ with $PC_{61}BM$, the PCE of the device increases to 1.76% due to the higher V_{oc} and J_{sc}. Further device optimization can be realized by the thermal annealing on the devices at temperature from 70 to 160 °C for 10 min, and the highest PCE values of 2.59% is obtained when the annealing temperature is 160 °C (**Figure S10a** and **Table S2**). The enhanced performance upon thermal annealing can be attributed to the improvement in J_{sc} which is correlated to the improved morphology of the active layer for the absorption enhancement (see **Figure S11**). Moreover, the SMSCs based on BDT(TBTTT6)$_2$ as donor and $PC_{61}BM$ or $PC_{71}BM$ as acceptor at the D/A weight ratio of 1:0.8 were also tested. Different from the BDT(TffBTTT6)$_2$ based devices, blending BDT(TBTTT6)$_2$ with $PC_{71}BM$ as active layer in the device shows a better PCE than BDT(TBTTT6)$_2$/$PC_{61}BM$-based one (1.3% *vs* 1.06%). The contrary impact caused by the acceptors is due to the different morphology (discussed later). Similarly, thermal annealing plays positive effect on the devices based on BDT(TBTTT6)$_2$/$PC_{71}BM$, and an optimized PCE of 1.8% is achieved after annealed at 100 °C for 10 min (see **Figure S10b** and **Table S2**).

Although the progress has been made in the device performance upon thermal treatment, the PCEs are still very low relative to those of most reported SMSCs. It has been reported that the addition of the process additives to the blend solution before spin-casting into the films significantly affects the efficiency of the resulting organic solar cells. As a solvent additive, diiodooctane (DIO) has been used during the film-casting step to further optimization of the photovoltaic performance. At present, there is no reported literature about the application of DIO in inverted devices though it plays a good role in many conventional small molecule devices. Here, 0.5, 1.0 and 2.0 v/v% of DIO concentrations in chloroform were used to optimize the devices. The photovoltaic performance data of the OSCs are provided in **Figure S12** and **Table S3**. As the concentration of DIO is increased, the V_{oc} tends to decrease. While this phenomenon remains unexplained, it is consistent with previous reports.[44-46] When addition of 0.5 v/v% DIO into the active layer, the devices with the two SMs show a significant improvement in photovoltaic performance. The PCE is improved to 3.11% for BDT(TffBTTT6)$_2$/$PC_{61}BM$ and to 2.82% for BDT(TBTTT6)$_2$/$PC_{71}BM$ with remarkably enhanced J_{sc} and FF. The significant improved efficiency originates from the favorably morphological evolution in the active layer induced by DIO additive. Delightfully, the photovoltaic performance is found to be further improved with addition of 0.5 v/v% DIO, followed by thermal annealing within the temperature range of 70 to 170 °C for 10 min. As shown in **Figure S13 and Table S4**, the SMSC based on the fluorinated molecule BDT(TffBTTT6)$_2$ demonstrates the best PCE of 4.17%, which is the highest reported value for the solution-processed inverted SMSCs based on BDT and BT unit. The nonfluorinated BDT(TBTTT6)$_2$ also shows an improved PCE of 3.17%. In addition, compared to the BDT(TBTTT6)$_2$-based devices, BDT(TffBTTT6)$_2$-based ones achieve the higher device parameters including V_{oc}, J_{sc} and FF. The improved V_{oc} comes from the lower HOMO levels by incorporation of F atoms, and the broader response range and more favorable morphology should be responsible for the J_{sc} and FF enhancement.

The external quantum efficiency (EQE) spectra according to the *J-V* curves are shown in **Figure 5b**. The EQE peak of both BDT(TffBTTT6)$_2$ and BDT(TBTTT6)$_2$ significantly enhanced after optimizing by addition of DIO and thermal annealing, contribution to J_{sc} enhancement. All J_{sc} values calculated by EQE are quite in consistent with the values obtained from *J–V* curves. Moreover, with respect to that of BDT(TBTTT6)$_2$, the EQE spectrum of BDT(TffBTTT6)$_2$ shows a broader response and red-shift, which is in agreement with their UV absorption. Additionally, as shown in **Figure 5c**, the stability of the optimized devices of BDT(TffBTTT6)/$PC_{61}BM$ were tested. The devices without encapsulations were placed in glovebox for several days before measurement. The device with inverted structure only decrease 35% PCE value after constant preserve in glovebox for a long time of 49

days, which exhibit a good stability compare to most reported small molecules in conventional device. The decrease of PCE mainly result from the J_{sc} and FF slowly decaying. The *J*–*V* characteristics of this long-term stable device as a function of time can be seen in **Figure S14.**

2.7. Grazing incident X-ray diffraction (GIXRD). To further investigate the reason behind the significant improvement in photovoltaic performance after optimizing the device by the addition of DIO and thermal annealing, grazing incident X-ray diffraction (GIXRD) was applied to probe the structure order/molecular packing in these BHJ films. Comparing diffraction patterns in out-of-plane cut (**Figure 6**) with the in-plane cut (**Figure S15**), both of the blend films only exhibit diffraction peak located at the low angles in out-of-plane cut, implying an edge-on orientation of donor materials. Shown in **Figure 6**, the pristine BDT(TBTTT6)$_2$/PC$_{71}$BM blend film displays a weak (100) diffraction peak located at 3.71° in out-of-plane cut, corresponding to the d-spacing of 2.64 nm between the molecular layers. After optimized with 0.5% DIO and thermal annealing, the (100) peak shifts to 4.04° and becomes much stronger, indicating an improved layer packing of the molecules existing in the BHJ film. The enhanced degree of crystallization can improve the phase purity and intermix phase area of the materials, which make positive effects on device performance. The change in the morphology of BDT(TffBTTT6)$_2$/PC$_{61}$BM film is similar with that in BDT(TBTTT6)$_2$/PC$_{71}$BM film, as shown in **Figure 6**. Compared with the BDT(TBTTT6)$_2$/PC$_{71}$BM pristine film, BDT(TffBTTT6)$_2$/PC$_{61}$BM pristine film shows a (100) diffraction peak at 4.23°, corresponding to a shorter d-spacing of 2.32 nm. This suggests that the fluorinated BDT(TffBTTT6)$_2$ forms denser molecular packing than the nonfluorinated counterpart, in accordance with the XRD and UV observation. As the same to BDT(TBTTT6)$_2$/PC$_{71}$BM film, the addition of DIO and thermal annealing improve the degree of crystallization of BDT(TffBTTT6)$_2$/PC$_{61}$BM film to form a well-intermixed phase, as revealed by the upshift (100) diffraction peak from 4.23° to 4.87° with strongly increased intensity. It can be inferred that the dense molecular packing of BDT(TffBTTT6)$_2$ may induce macrophase separation between donor and acceptor in the pristine blend films, at the same time, combination of addition of DIO and thermal annealing promotes a well-intermixed microphase morphology in active film for more efficient charge transfer and transportation.

2.8. Morphologies of the Active Layers. The morphological change can be clearly detected by the transmission electron microscopy (TEM). **Figure 7** shows the morphology of BDT(TffBTTT6)$_2$/PC$_{61}$BM and BDT(TBTTT6)$_2$/PC$_{71}$BM films with or without optimization, and the bright and dark regions correspond to donors and PC$_{61}$BM or PC$_{71}$BM-rich domains, respectively.[47-49] Owing to the good miscibility of BDT(TffBTTT6)$_2$ and PC$_{61}$BM, BDT(TBTTT6)$_2$ and PC$_{71}$BM, two very uniform and homogenous morphology of corresponding pristine films are observed in **Figure 7a** and **c**. However, the BDT(TffBTTT6)$_2$ and PC$_{61}$BM, BDT(TBTTT6)$_2$ and PC$_{71}$BM are mixed so well that a desirable nanostructure with separated donor and acceptor domains are not obtained. Upon optimization of 0.5 v/v% DIO and 70 °C annealing, the domain size of each component becomes bigger and a nano-scale phase separation is developed in **Figure 7b** and **d**, and the BDT(TffBTTT6)$_2$-based film exhibit better nano-scale phase separation as well as better donor/acceptor interpenetrating network due to the existence of fluorine atoms, consequently leading to the dramatically improved device performance. These results are well consistent with the GIXRD measurement. Furthermore, from the **Figure S16**, we can also see that BDT(TffBTTT6)$_2$ has better miscibility with PC$_{61}$BM than PC$_{71}$BM, while BDT(TBTTT6)$_2$ presents the opposite behavior. Therefore, BDT(TffBTTT6)$_2$/PC$_{61}$BM and BDT(TBTTT6)$_2$/PC$_{71}$BM films shows better performance than their counterparts.

The tapping-mode atomic force microscopy (AFM) was used to study the surface morphology of the active Layers. The AFM height and phase images of the blend films in **Figure 8** demonstrate the morphological evolution in the active layer induced by DIO additive and thermal annealing. The root-mean-square (RMS) roughness of the BDT(TffBTTT6)$_2$/PC$_{61}$BM and BDT(TBTTT6)$_2$/PC$_{71}$BM films without any processing are 4.49 nm and 0.36 nm,

respectively. When the BHJ blend films processed with 0.5% DIO and 70 °C annealing, the AFM images show that the RMS of BDT(TffBTTT6)$_2$/PC$_{61}$BM and BDT(TBTTT6)$_2$/PC$_{71}$BM films increased to 12.0 nm and 4.50 nm, respectively. The relative coarse surface morphology in the processed film could be attributed to the rearrangement of the SMs in the BHJ blend, as frequently reported for DIO processed polymer/fullerene films.[50,51] Similar to the observation from TEM and GIXRD, the DIO additive and thermal annealing can induce the self-organized ordering or the crystalline domain of the BDT(TffBTTT6)$_2$/PC$_{61}$BM and BDT(TBTTT6)$_2$/PC$_{71}$BM. The phase images in **Figure 8** illustrate that the donor/acceptor interpenetrating network of the blend film of BDT(TffBTTT6)$_2$/PC$_{61}$BM is better than that of BDT(TBTTT6)$_2$/PC$_{71}$BM, which could be due to the existence of the F atoms. Therefore, the better photovoltaic performance of the BDT(TffBTTT6)$_2$/PC$_{61}$BM active layer should be also related to the suitable morphology of the active layer.

2.9. Hole Mobility. The hole mobilities of the with and without optimized blend of BDT(TffBTTT6)$_2$/PC$_{61}$BM and BDT(TBTTT6)$_2$/PC$_{71}$BM were measured by the Space-charge-limited current (SCLC) method[52] with a hole-only device structure of ITO/PEDOT:PSS/active layer/MoO_3/Ag, as shown in **Figure 9**. Without optimizing, the mobilities are 4.32 × 10^{-4} cm^2 V^{-1} s^{-1} for BDT(TffBTTT6)$_2$ device that higher than 2.59 × 10^{-4} cm^2 V^{-1} s^{-1} for BDT(TBTTT6)$_2$ device, due to the introduction of two F atoms. After optimizing with 0.5 v/v% DIO and 70 °C annealing, the mobilities increase to 8.71 × 10^{-4} cm^2 V^{-1} s^{-1} for BDT(TffBTTT6)$_2$ and to 4.9 × 10^{-4} cm^2 V^{-1} s^{-1} for BDT(TBTTT6)$_2$ device. The difference in the hole mobilities of BDT(TffBTTT6)$_2$ and BDT(TBTTT6)$_2$ device also can partly explain the variation in the device performance.

3. Conclusions

In summary, two small molecules BDT(TffBTTT6)$_2$ and BDT(TBTTT6)$_2$ with the A-D-A structure and BDT as the donor unit while BT as the acceptor unit have been designed and synthesized. After introducing two F atoms on the benzothiadiazole unit, the molecular energy level, packing and charge-carrier transport capability of the BDT(TffBTTT6)$_2$ have been finely tuned, resulting in a higher V_{oc}, J_{sc}, FF of BDT(TffBTTT6)$_2$-based device compared to those of nonfluorinated molecule. Further optimization by DIO and thermal annealing, the fluorinated small molecules-based devices shows dramatically improved device performance due to promote more favorable morphology evolution of active layer and BDT(TffBTTT6)$_2$-based inverted device achieves a notable PCE of 4.17%. To our best knowledge, the PCE of 4.17% is the highest value of solution processed SMSCs fabricated from BDT-BT-based SMs. Moreover, fluorinated small molecules show more favorable morphology after solvent additive process, so this strategy can be as an effective way for the development of fluorinated small molecules in stabilized inverted-based SMSCs.

4. Experimental Section

Synthesis of 4-(5-Bromo-thiophen-2-yl)-5,6-difluoro-7-(5'-hexyl-[2,2']bithiophenyl-5-yl)benzo[1,2,5]thiadiazole (4). A solution of compound 1 (1.11 g, 2.43 mmol) and compound 2 (1.20 g, 2.43 mmol) in dry toluene (20 mL) was degassed thrice with nitrogen followed by the addition of Pd(PPh$_3$)$_4$ (150 mg, 0.13 mmol). After being stirred at 85 °C for 12 h under nitrogen, the reaction mixture was cooled to room temperature and then dissolved in CH_2Cl_2, washed with water and dried by anhydrous magnesium sulfate. After evaporation of the solvent, the crude product was purified by column chromatography on silica gel using a mixture of dichloromethane and petroleum ether (1:8) as eluant to afford compound 4 (0.78 g, 55%) as a red solid. ^{1}H NMR (400 MHz, $CDCl_3$) δ (ppm): 8.18 (d, 1H), 8.0 (d, 1H), 7.20 (m, 2H), 7.13 (d, 1H), 6.72 (d,1H), 2.81 (m, 2H), 1.70 (m, 2H), 1.56 (m, 2H), 1.25-1.34 (m, 4H), 0.90 (t, 3H). ^{13}C NMR (400 MHz, $CDCl_3$) δ (ppm): 148.43, 146.64, 141.31, 134.09, 131.97, 130.18, 125.17, 124.07, 122.97, 116.54, 109.72, 31.47, 30.05, 28.65, 22.56, 17.13, 13.92.

Synthesis of BDT(TffBTTT6)$_2$. A solution of compound 4 (400 mg, 0.69 mmol) and 6 (250 mg, 0.28 mmol) in dry toluene (10 mL) was degassed thrice with nitrogen followed by the addition of $Pd(PPh_3)_4$ (17.3 mg, 0.015 mmol). After the reaction stirred at 100 °C for 24 h under a nitrogen atmosphere, the reaction mixture was cooled to room temperature and then dissolved in chloroform, washed with water and dried by anhydrous magnesium sulfate. After removal of the solvent, the crude product was purified by column chromatography on silica gel using chloroform and petroleum ether (3:1) as eluant to obtain a metallic purple solid. The crude product was recrystallized from chloroform and petroleum ether three times to afford BDT(TffBTTT6)$_2$ (330 mg, 75%) as a metallic purple solid and characterized by HTGC (>99%). ^{1}H NMR (400 MHz, $CDCl_3$) δ (ppm): 7.67 (m, 4H), 6.96 (m, 4H), 6.70 (m, 6H), 6.44 (m, 4H), 3.01 (d, 4H), 2.57 (t, 4H), 1.85 (m, 2H), 1.25-1.51 (m, 32H), 0.88-1.12 (m, 18H). MS (MALDI-FTMS) m/z: Calculated for $C_{82}H_{78}F_4N_4S_{12}$ $[M+1]^+$， 1578.28； found 1578.3.

The synthesis and purification processes of 5 are similar with those of 4, but monomer 2 was used instead of 3. The obtained product 5 is a red solid with ca. 50% yield. ^{1}H NMR (400 MHz, $CDCl_3$) δ (ppm): 8.02 (d, 1H), 7.75-7.81 (m, 3H), 7.17 (m, 2H), 7.09 (d, 1H), 6.71 (d, 1H), 2.81 (m, 2H), 1.70 (m, 2H), 1.31-1.53 (m, 6H), 0.90 (t, 3H). ^{13}C NMR (400MHz, $CDCl_3$) δ (ppm): 152.03, 146.16, 142.71, 140.60, 139.82, 134.49, 130.64, 128.50, 126.99, 125.87, 125.20, 124.86, 123.83, 123.81, 114.36, 31.55, 30.23, 28.75, 22.56, 14.07.

The synthesis and purification processes of BDT(TBTTT6)$_2$ are similar with those of BDT(TffBTTT6)$_2$, but monomer 5 was used instead of 4. The obtained BDT(TBTTT6)$_2$ is also a metallic purple solid with ca. 80% yield. ^{1}H NMR (400 MHz, $CDCl_3$) δ (ppm): 7.72 (m, 4H), 7.48 (m, 4H), 7.29 (s, 2H), 6.97 (m, 2H), 6.88 (m, 2H), 6.56-6.59 (m, 4H), 2.98 (d, 4H), 2.70 (t, 4H), 1.82 (m, 2H), 1.46-1.61 (m, 32H), 0.88-1.09 (m, 18H). MS (MALDI-FTMS) m/z: Calculated for $C_{82}H_{82}N_4S_{12}$ $[M+1]^+$， 1506.32； found 1507.3.

Fabrication and Characterization of OSCs. Organic solar cells (OSCs) were fabricated in the configuration of the traditional sandwich structure of ITO/ZnO/photoactive layer/MoO_3/Ag. ITO-coated glass was cleaned by ultrasonic agitation in acetone, detergent, deionized water and isopropanol sequentially followed by UV treating for 20 min. Then the ZnO precursor solution was spin-cast on the ITO glass at 4000 rpm for 1 min and annealed at 205 °C for 1 h in air to yield a approximately 30 nm film thickness. The devices were transferred into a glovebox filled with N_2. The active layer was prepared by spin-cast the solution of the organic compounds donor (D) and $PC_{61}BM$ or $PC_{71}BM$ acceptor (A) with different D/A ratios on the top of the ZnO layer . The concentration of the solution was 18 mg/mL in chloroform (CF) (or with different volume of DIO). Then the device was annealed at different temperature for 10 min. Finally, the MoO_3 (7 nm)/Ag (90 nm) was vacuum evaporated on the active layer under a shadow mask in the vacuum of ca. 10^{-4} pa. The active layer area of the device is 4 mm^2. The light source was calibrated by using silicon reference cells with an AM 1.5 Global solar simulator with an intensity of 100 mW/cm^2. The current -voltage (*J-V*) characteristics were measured with a Keithley 2400 source meter (Abet Solar Simulator Sun 200). All the measurements were performed under ambient atmosphere at room temperature. The EQE was measured under monochromatic illumination (Oriel Cornerstone 260 1/4 monochromator equipped with Oriel 70613NS QTH lamp), and the calibration of the incident light was performed with a monocrystalline silicon diode.

Electronic Supplementary Information (ESI) available

The detailed experimental sections and the corresponding characterization are in Supporting Information.

Acknowledgements

This work was financially supported by the National Science Fund for Distinguished Young Scholars (51425304), National Natural Science Foundation of China (51263016, 51473075 and 21402080), National Basic Research Program of China (973 Program 2014CB260409), and the Natural Science Foundation of Jiangxi Province (20143ACB20001 and 20151BAB203016).

References:

1 J. Y. Kim, K. Lee, N. E. Coates, D. Moses, T.-Q. Nguyen, M. Dante and A. J. Heeger, *Science* 2007, **317**, 222-225.

2 B. C. Thompson and J. M. J. Fréchet, *Angew. Chem. Int. Edi.* 2008, **47**, 58-77.

3 Y.-J. Cheng, S.-H. Yang and C.-S. Hsu, *Chem. Rev.* 2009, **109**, 5868-5923.

4 H. Zhou, L. Yang and W. You, *Macromolecules* 2012, **45**, 607-632.

5 Y. Lin, Y. Li and X. Zhan, *Chem. Soc. Rev.* 2012, **41**, 4245-4272.

6 J. You, L. Dou, K. Yoshimura, T. Kato, K. Ohya, T. Moriarty, K. Emery, C. C. Chen, J. Gao, G. Li and Y. Yang, *Nat Commun.* 2013, **4**, 1446.

7 C. C. Chen, W. H. Chang, K. Yoshimura, K. Ohya, J. You, J. Gao, Z. Hong and Y. Yang, *Adv. Mater.* 2014, **26**, 5670-5677.

8 Y. Liu, J. Zhao, Z. Li, C. Mu, W. Ma, H. Hu, K. Jiang, H. Lin, H. Ade and H. Yan, *Nat. Commun.* 2014, **5**, 5293.

9 H. Kang, S. Kee, K. Yu, J. Lee, G. Kim, J. Kim, J. R. Kim, J. Kong and K. Lee, *Adv. Mater.* 2015, **27**, 1408-1413.

10 J. Roncali, *Accounts of chemical research* 2009, **42**, 1719-1730.

11 B. Walker, C. Kim and T.-Q. Nguyen, *Chem. Mater.* 2011, **23**, 470-482.

12 J. Roncali, P. Leriche and P. Blanchard, *Adv. Mater.* 2014, **26**, 3821-3838.

13 Q. Zhang, B. Kan, F. Liu, G. Long, X. Wan, X. Chen, Y. Zuo, W. Ni, H. Zhang, M. Li, Z. Hu, F. Huang, Y. Cao, Z. Liang, M. Zhang, T. P. Russell and Y. Chen, *Nat. Photonics* 2014, **9**, 35-41.

14 B. Kan, M. Li, Q. Zhang, F. Liu, X. Wan, Y. Wang, W. Ni, G. Long, X. Yang, H. Feng, Y. Zuo, M. Zhang, F. Huang, Y. Cao, T. P. Russell and Y. Chen, *J. Am. Chem. Soc.* 2015, **137**, 3886-3893.

15 J. Zhou, Y. Zuo, X. Wan, G. Long, Q. Zhang, W. Ni, Y. Liu, Z. Li, G. He, C. Li, B. Kan, M. Li and Y. Chen, *J. Am. Chem. Soc.* 2013, **135**, 8484-8487.

16 J. Zhou, X. Wan, Y. Liu, Y. Zuo, Z. Li, G. He, G. Long, W. Ni, C. Li, X. Su and Y. Chen, *J. Am. Chem. Soc.* 2012, **134**, 16345-16351.

17 B. Kan, Q. Zhang, M. Li, X. Wan, W. Ni, G. Long, Y. Wang, X. Yang, H. Feng and Y. Chen, *J. Am. Chem. Soc.* 2014, **136**, 15529-15532.

18 S. Shen, P. Jiang, C. He, J. Zhang, P. Shen, Y. Zhang, Y. Yi, Z. Zhang, Z. Li and Y. Li, *Chem. Mater.* 2013, **25**, 2274-2281.

19 Y. Chen, Z. Du, W. Chen, Q. Liu, L. Sun, M. Sun and R. Yang, *Org. Electron.* 2014, **15**, 405-413.

20 Y. Sun, G. C. Welch, W. L. Leong, C. J. Takacs, G. C. Bazan and A. J. Heeger, *Nat. Mater.* 2012, **11**, 44-48.

21 T. S. van der Poll, J. A. Love, T. Q. Nguyen and G. C. Bazan, *Adv. Mater.* 2012, **24**, 3646-3649.

22 P. Dutta, J. Kim, S. H. Eom, W. H. Lee, I. N. Kang and S. H. Lee, *ACS Appl. Mater. Interfaces* 2012, **4**, 6669-6675.

23 H.-F. Feng, W.-F. Fu, L. Li, Q.-C. Yu, H. Lu, J.-H. Wan, M.-M. Shi, H.-Z. Chen, Z. a. Tan and Y. Li, *Org. Electron.* 2014, **15**, 2575-2586.

24 Y. S. Choi, T. J. Shin and W. H. Jo, *ACS Appl. Mater. Interfaces* 2014, **6**, 20035-20042.

25 Z. He, C. Zhong, X. Huang, W. Y. Wong, H. Wu, L. Chen, S. Su and Y. Cao, *Adv. Mater.* 2011, **23**, 4636-4643.

26 H.-Y. Chen, J. Hou, S. Zhang, Y. Liang, G. Yang, Y. Yang, L. Yu, Y. Wu and G. Li, *Nat. Photonics* 2009, **3**, 649-653.

27 M. M Shi, L. Fu, X. L. Hu, L. J. Zuo, D. Deng, J. Chen and H. Z Chen, *Polym. Bull.* 2012, **68,** 1867-1877.

28 R. C. Coffin, J. Peet, J. Rogers, G. C. Bazan, *Nat. Chemistry* 2009, **1**, 657-661.

29 A. J. Moulé, A. Tsami, T. W. Bünnagel, M. Forster, N. M. Kronenberg, M.; Koppe, M. Scharber, M. Morana, C. J. Brabec, K. Meerholz, *Chem. Mater.* 2008, **20**, 4045-4050.

30 A. C. Stuart, J. R. Tumbleston, H. Zhou, W. Li, S. Liu, H. Ade and W. You, *J. Am. Chem. Soc.* 2013, **135**, 1806-1815.

31 B. C. Schroeder, Z. Huang, R. S. Ashraf, J. Smith, P. D'Angelo, S. E. Watkins, T. D. Anthopoulos, J. R. Durrant and I. McCulloch, *Adv. Funct. Mater.* 2012, **22**, 1663-1670.

32 Z. Li, J. Lu, S.-C. Tse, J. Zhou, X. Du, Y. Tao and J. Ding, *J. Mater. Chem.* 2011, **21**, 3226.

33 H. J. Son, W. Wang, T. Xu, Y. Liang, Y. Wu, G. Li and L. Yu, *J. Am. Chem. Soc.* 2011, **133**, 1885-1894.

34 S. C. Price, A. C. Stuart, L. Yang, H. Zhou and W. You, *J. Am. Chem. Soc.* 2011, **133**, 4625-4631.

35 Y. Zhang, J. Zou, C.-C. Cheuh, H.-L. Yip and A. K. Y. Jen, *Macromolecules* 2012, **45**, 5427-5435.

36 S. Albrecht, S. Janietz, W. Schindler, J. Frisch, J. Kurpiers, J. Kniepert, S. Inal, P. Pingel, K. Fostiropoulos, N. Koch and D. Neher, *J. Am. Chem. Soc.* 2012, **134,** 14932-14944.

37 H. Zhou, L. Yang, A. C. Stuart, S. C. Price, S. Liu and W. You, *Angew. Chem. Int. Ed. Engl.* 2011, **50**, 2995-2998.

38 J. R. Tumbleston, A. C. Stuart, E. Gann, W. You and H. Ade, *Adv. Funct. Mater.* 2013, **23**, 3463-3470.

39 W. Li, S. Albrecht, L. Yang, S. Roland, J. R. Tumbleston, T. McAfee, L. Yan, M. A. Kelly, H. Ade, D. Neher and W. You, *J. Am. Chem. Soc.* 2014, **136**, 15566-15576.

40 Z. B. Henson, G. C. Welch, T. van der Poll and G. C. Bazan, *J. Am. Chem. Soc.* 2012, **134**, 3766-3779.

41 M. M. M. Raposo, A. M. c. C. Fonseca and G. Kirsch, *Tetrahedron* 2004, **60**, 4071-4078.

42 C. Risko, M. D. McGehee and J.-L. Brédas, *Chem. Sci.* 2011, **2**, 1200-1218.

43 Q. Peng, S. L. Lim, I. H. Wong, J. Xu and Z. K. Chen, *Chemistry* 2012, **18**, 12140-12151.

44 J. A. Love, S. D. Collins, I. Nagao, S. Mukherjee, H. Ade, G. C. Bazan, and T. Q. Nguyen, *Adv. Mater.* 2014, 26, 7308–7316.

45 Y. Sun, G. C. Welch, W. L. Leong, C. J. Takacs, G. C. Bazan, A. J. Heeger, *Nat. Mater.* **2011**, 1, 44.

46 J. A. Love, I. Nagao, Y. Huang, M. Kuik, V. Gupta, C. J. Takacs, J. E. Coughlin, L. Qi, T. S. van der Poll, E. J. Kramer, A. J. Heeger, T.-Q. Nguyen, G. C. Bazan, J. Am. Chem. Soc. 2014, 136, 3597.

47 M. Zhang, X. Guo, S. Zhang and J. Hou, *Adv Mater* 2014, **26**, 1118-1123.

48 M. S. Su, C. Y. Kuo, M. C. Yuan, U. S. Jeng, C. J. Su and K. H. Wei, *Adv. Mater.* 2011, **23**, 3315-3319.

49 W. Ma, J. Y. Kim, K. Lee and A. J. Heeger, *Macromol. Rapid Commun.* 2007, **28**, 1776-1780.

50 L. Ye, S. Zhang, W. Ma, B. Fan, X. Guo, Y. Huang, H. Ade, J. Hou, *Adv. Mater.* 2012, **24**, 6335-6341.

51 H.-Y. Chen, H. Yang, G. Yang, S. Sista, R. Zadoyan, G. Li, Y. Yang, *J. Phys. Chem. C* 2009, **113**, 7946-7953.

52 G. Malliaras, J. Salem, P. Brock and C. Scott, *Phys. Rev. B* 1998, ***58***, R13411.

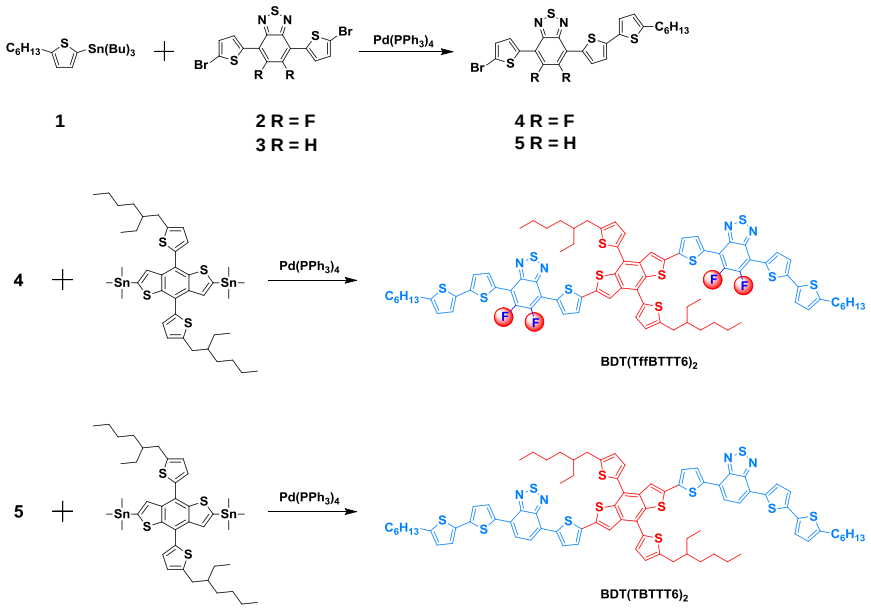

Scheme 1. Synthetic Route of $BDT(TffBTTT6)_2$ and $BDT(TBTTT6)_2$

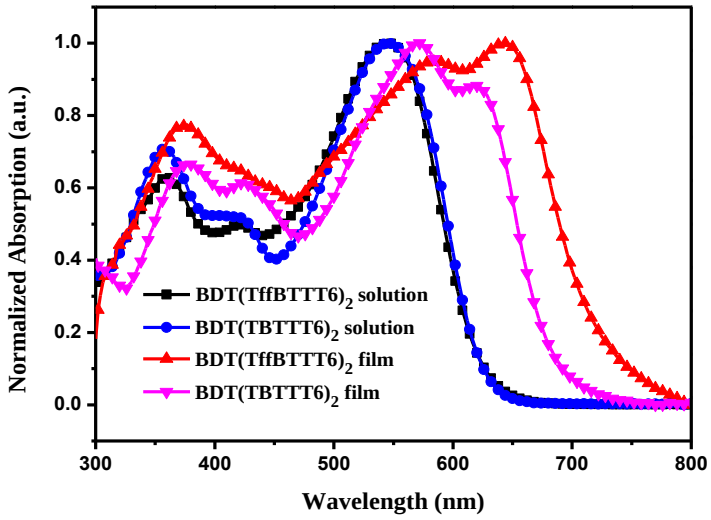

Figure 1. Normalized UV-vis absorption spectra of BDT(TffBTTT6)$_2$ and BDT(TBTTT6)$_2$ in chloroform solutions and in the film states.

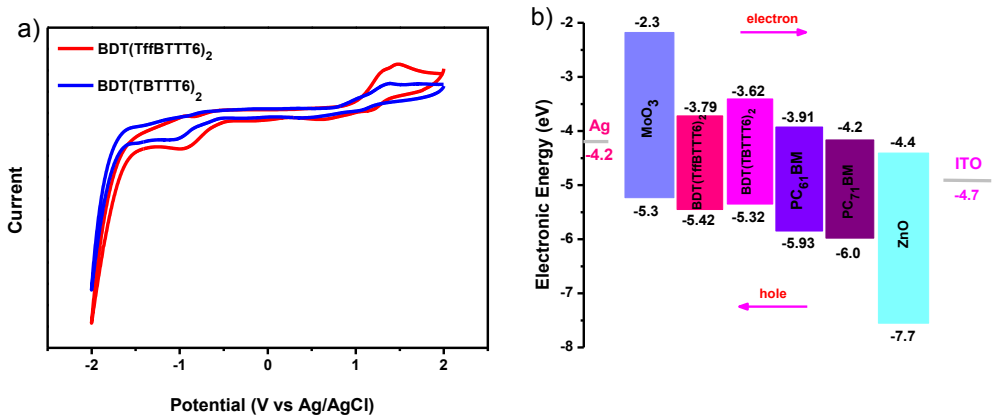

Figure 2. (a) Cyclic voltammogram of the BDT(TffBTTT6)$_2$ and BDT(TBTTT6)$_2$ film in a 0.1 mol/L Bu_4NPF_6/CH_3CN solution at a scan rate of 50 mV/s. (b) the HOMO and LUMO energy levels of BDT(TffBTTT6)$_2$, BDT(TBTTT6)$_2$, $PC_{61}BM$, $PC_{71}BM$, MoO_3, ZnO, and the work functions of the ITO cathode and Ag anode.

Table 1. Optical and Electrochemical Properties of Small Molecules (SMs)

SMs	UV-Vis Absorption			E_g^{opt} (eV)[b]	HOMO	LUMO (eV)	E_g^{cv} (eV)[c]
	λ_{max} (solution) (nm)[a]	λ_{max} (film) (nm)	λ_{onset} (film) (nm)		(eV)		
$BDT(TffBTTT6)_2$	544	642	769	1.61	-5.42	-3.79	1.63
$BDT(TBTTT6)_2$	546	572	714	1.74	-5.32	-3.62	1.70

[a]Measured in a $CHCl_3$ solution. [b]Determined from the onset of UV-Vis absorption spectra, $Eg^{opt} = 1240/\lambda_{onset}$. [c]Determined from cyclic voltammetry.

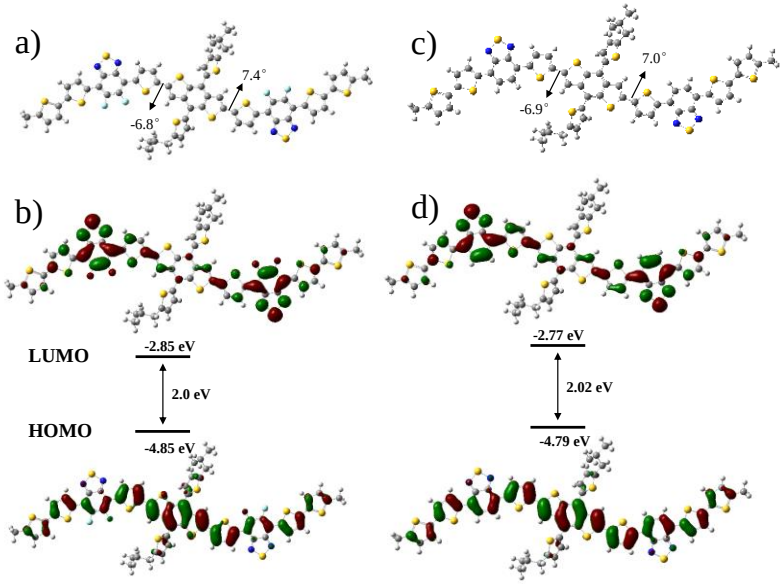

Figure 3. Optimized geometries with the lowest total energy of BDT(TffBTTT6)$_2$ (a) and BDT(TBTTT6)$_2$ (c). The HOMO/LUMO orbital energy diagrams and HOMO/LUMO energy levels of BDT(TffBTTT6)$_2$ (b) and (d) BDT(TBTTT6)$_2$.

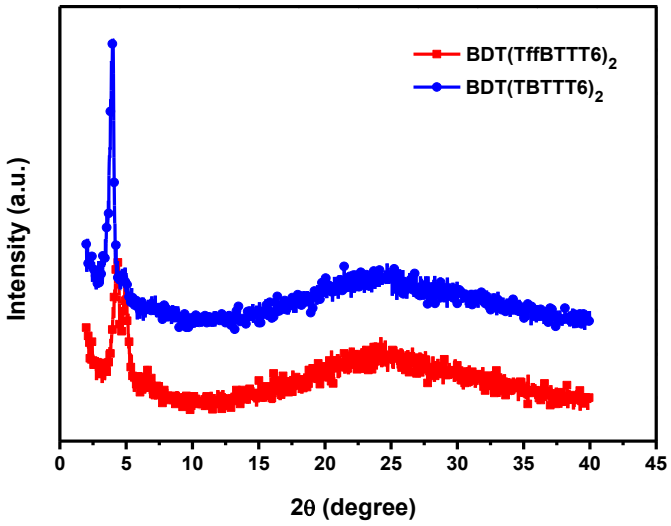

Figure 4. XRD patterns of BDT(TffBTTT6)$_2$ and BDT(TBTTT6)$_2$ films.

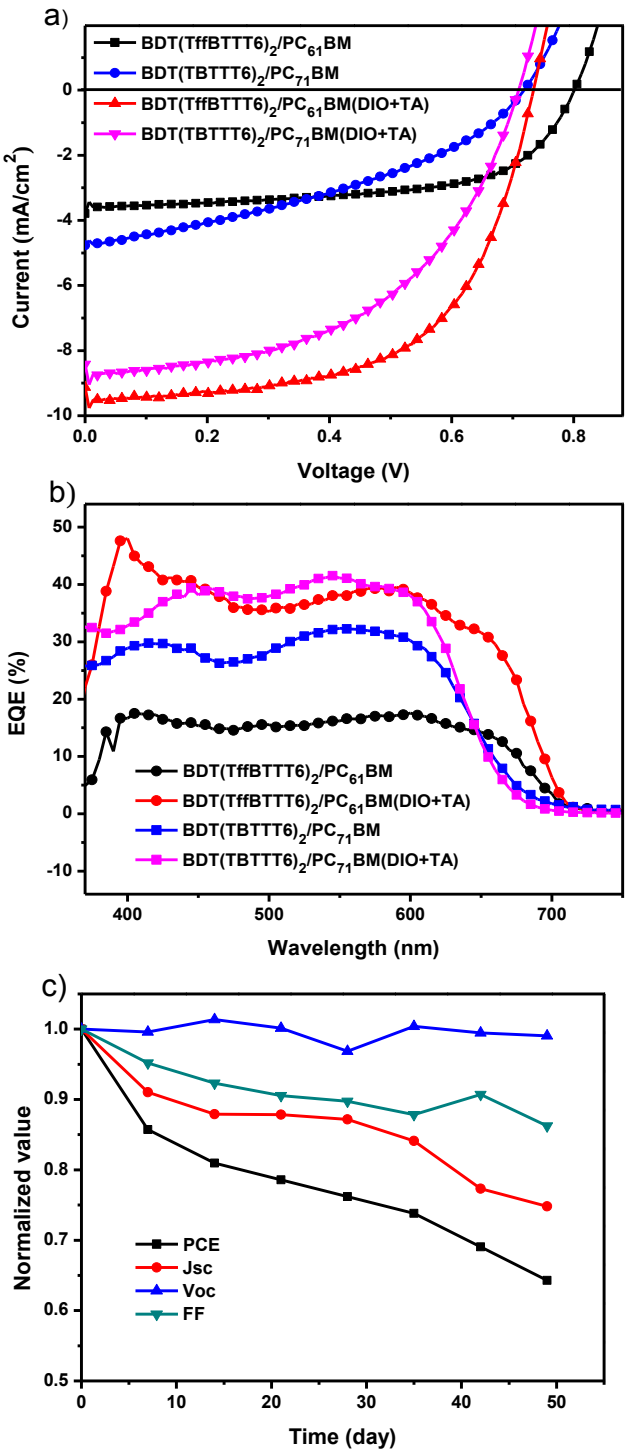

Figure 5. (a) *J-V* curves of solar cells with an active layer composed of BDT(TffBTTT6)$_2$/PC$_{61}$BM and BDT(TBTTT6)$_2$/PC$_{71}$BM with or without optimizing by 0.5 v/v% DIO and 70 °C annealing. (b) EQE plots of solar cells with an active layer composed of BDT(TffBTTT6)$_2$/PC$_{61}$BM and BDT(TBTTT6)$_2$/PC$_{71}$BM with or without optimizing by 0.5 v/v% DIO and 70 °C annealing (TA). (c) Normalized PCE decay of devices: ITO/ZnO/BDT(TffBTTT6)$_2$:PC$_{61}$BM /MoO$_3$/Ag at glovebox.

Table 2. Device Performance Parameters for BHJ Solar Cells Based on BDT(TffBTTT6)$_2$ and BDT(TBTTT6)$_2$

Active layer[a]	V_{oc} (V)	J_{sc} (mA cm^{-2})	FF (%)	PCE$_{max}$(avg)[b] (%)
BDT(TffBTTT6)$_2$/PC$_{61}$BM	0.8	3.79	58.0	1.76 (1.71)
BDT(TffBTTT6)$_2$/PC$_{71}$BM	0.73	2.97	59.8	1.3 (1.26)
BDT(TffBTTT6)$_2$/PC$_{61}$BM (DIO+TA)[c]	**0.73**	**9.13**	**62.5**	**4.17 (3.97)**
BDT(TBTTT6)$_2$/PC$_{61}$BM	0.72	4.25	34.6	1.06 (0.97)
BDT(TBTTT6)$_2$/PC$_{71}$BM	0.72	4.77	37.9	1.3 (1.21)
BDT(TBTTT6)$_2$/PC$_{71}$BM (DIO+TA)[c]	**0.71**	**8.42**	**53.0**	**3.17 (3.0)**

[a]Donor:acceptor weight ratio in active layer = 1:0.8. [b]Average values of ten devices. [c]DIO (0.5 v/v%) was added to the active-material solution and then the devices are annealed at 70 °C for 10 min (TA).

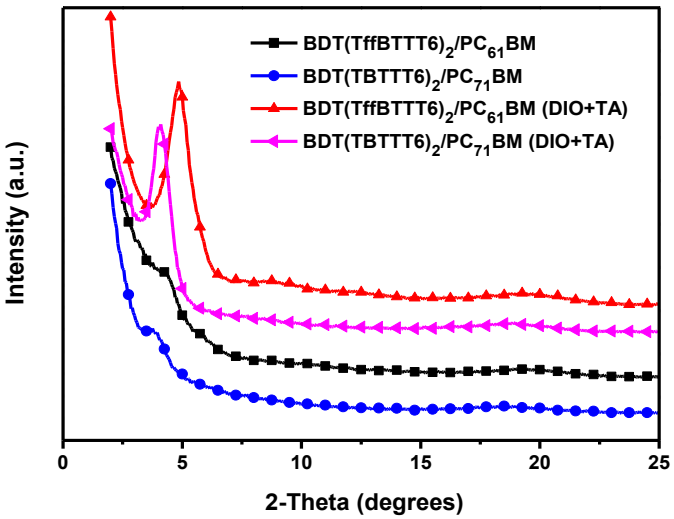

Figure 6. Out-of-plane grazing incident X-ray diffraction (GIXRD) measurement of BDT(TffBTTT6)$_2$/PC$_{61}$BM and BDT(TBTTT6)$_2$/PC$_{71}$BM film with or without 0.5 v/v% DIO and 70 °C annealing (TA).

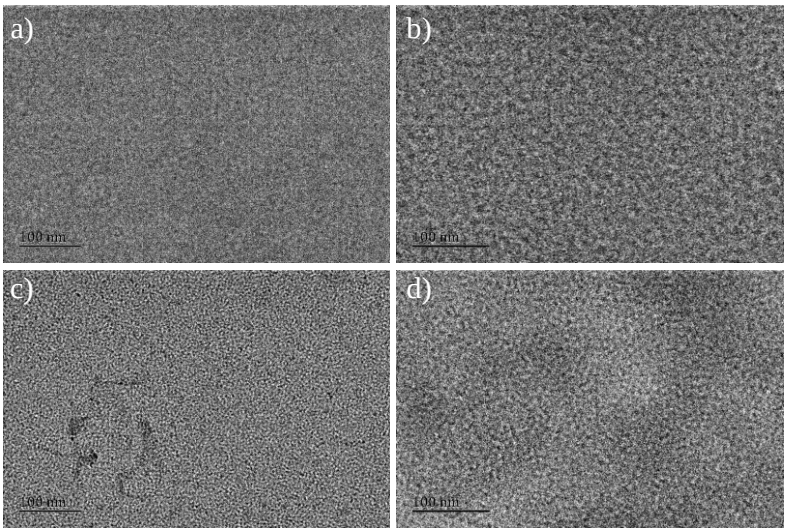

Figure 7. TEM images of the active layers with (a) BDT(TffBTTT6)$_2$/PC$_{61}$BM, (b) BDT(TffBTTT6)$_2$:PC$_{61}$BM with 0.5 v/v% DIO and 70 °c annealing, (c) BDT(TBTTT6)$_2$/PC$_{71}$BM, (d) BDT(TBTTT6)$_2$/PC$_{71}$BM with 0.5 v/v% DIO and 70 °c annealing . The scale bar is 100 nm.

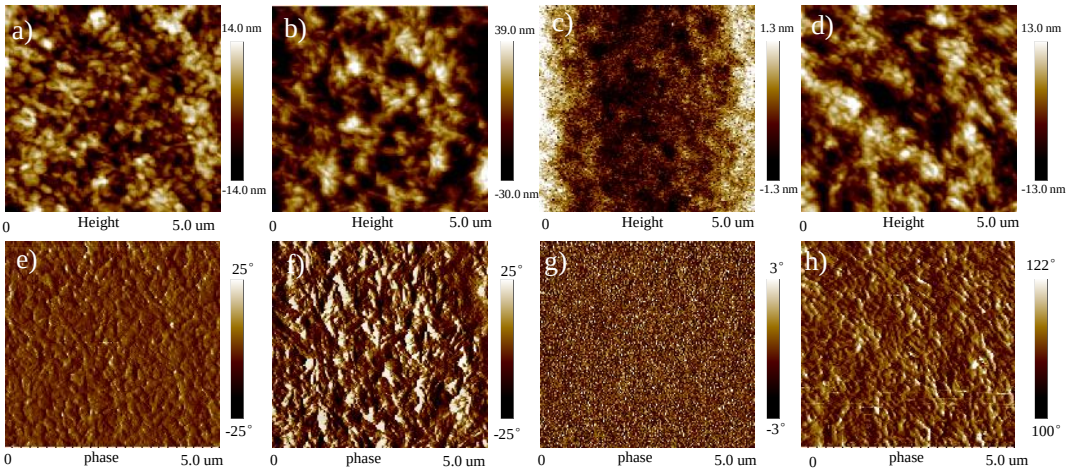

Figure 8. AFM height images (5 um × 5 um) (top) and phase images (bottom) of the active layers with BDT(TffBTTT6)$_2$/PC$_{61}$BM (a), (e); BDT(TffBTTT6)$_2$:PC$_{61}$BM with 0.5 v/v% DIO and 70 °c annealing (b), (f); BDT(TBTTT6)$_2$/PC$_{71}$BM (c), (g) and BDT(TBTTT6)$_2$/PC$_{71}$BM with 0.5 v/v% DIO and 70 °c annealing (d), (h).

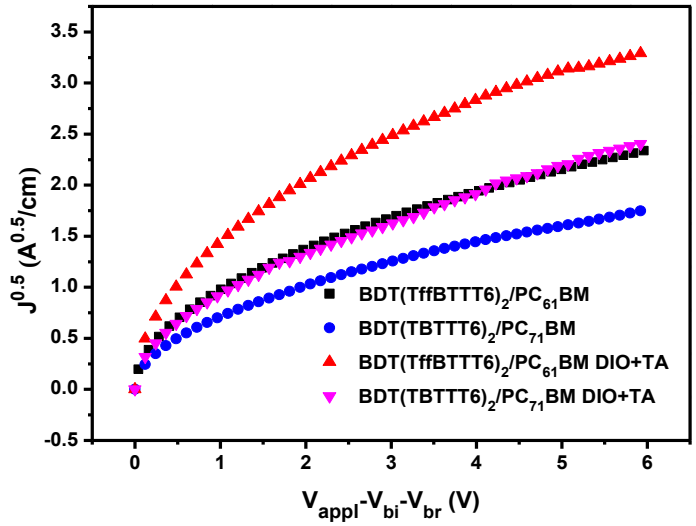

Figure 9. $J^{0.5}$–V plots of hole-only devices with an active layer composed of BDT(TffBTTT6)$_2$/PC$_{61}$BM and BDT(TBTTT6)$_2$/PC$_{71}$BM with or without optimizing by 0.5 v/v% DIO and 70 °C annealing (TA).

Table of Content

Solution-Processed Small Molecules Based on Benzodithiophene and Difluorobenzothiadiazole for Inverted Organic Solar Cells

Xunfan Liao[a], Feiyan Wu[a], Lie Chen*[a,b] and Yiwang Chen[a,b]

Fluorinated BDT(TffBTTT6)2 and nonfluorinated BDT(TBTTT6)2 are designed and synthesized to extensively investigate the effect of fluorination in small molecules.